Advanced Materials Technologies

ADVANCED MATERIALS TECHNOLOGIES
www.advmattechnol.com

RESEARCH ARTICLE OPEN ACCESS

Testing and Simulation of Multilayer Polyvinylidene Fluoride-Based Piezoelectric Energy Harvester Devices

Hamdi Ezzin[1] | Silvia Monchetti[1] | Paolo Emilio Puddu[2,3] | Luciano Teresi[4] | Antonio DeSimone[5] | Roberto Brighenti[1]

[1]Dept. of Civil & Environmental Engineering, Univ. of Florence, Florence, Italy | [2]Associazione per la Ricerca Cardiologica, Rome, Italy | [3]Unité EA 4650, Signalisation, électrophysiologie et imagerie des lésions d'ischémie reperfusion myocardique, Université De Caen Normandie, Caen, France | [4]Università Roma Tre, Roma, Italy | [5]BioRobotics Institute, Scuola Superiore Sant'Anna, Pontedera, Italy

Correspondence: Roberto Brighenti (roberto.brighenti@unifi.it)

Received: 3 March 2026 | **Revised:** 20 May 2026 | **Accepted:** 27 May 2026

Keywords: energy harvesting | implantable devices | kinematics of the heartbeat | piezoelectric polymers | polyvinylidene fluoride (PVDF)

ABSTRACT

Power supply challenges for implantable medical devices, including pacemakers and health sensors, require device miniaturization for safe and minimally invasive implantation, as well as advancements in energy supply and storage technologies, such as high-density batteries and wireless power transmission. Traditional piezoelectric energy harvesters (EH) often exhibit high electrical impedances, which can restrict their use in energy harvesting systems. To address this limitation, a polymer-based multilayer flexible energy harvesting device composed of alternating dielectric and piezoelectric β-phase polyvinylidene fluoride (PVDF) layers is introduced. A theoretical mechanical model based on large-displacement beam theory is developed to quantify the stress experienced by the piezoelectric layer, and parametric simulations of the generated energy are conducted. Experimental results are compared with simulation outcomes. Furthermore, using real human heart kinematics obtained from epicardium surface measurements, the voltage and energy obtainable from the proposed devices are evaluated. Compared to the single-layer configuration, the multilayer PVDF device demonstrates an increased maximum output voltage and capacitance, along with reduced impedance. The proposed EH multilayer PVDF-based provides significant advantages due to its simple and expandable architecture, indicating strong potential for supplying energy to small-scale devices for biomedical applications.

1 | Introduction

Implantable electronic devices have revolutionized modern medicine, enhancing diagnostic and therapeutic capabilities [1]. However, the power supply for these devices remains a critical challenge. Traditional implantable devices primarily rely on batteries, which have limitations such as finite energy density, limited lifespan, and potential chemical leakage. This necessitates additional surgeries after a limited number of years (typically 8–10 years for pacemakers, for instance) for battery replacement, with the consequence of increasing patient discomfort and healthcare costs. To address these issues, researchers have explored energy harvesting (EH) technologies to convert mechanical, thermal, and other forms of energy present in the human body or coming from the environment into electrical energy, aiming to achieve self-powered implantable devices (Figure 1). Among these technologies, energy harvesting based on piezoelectric (PZT) polymeric materials stands out due to its good efficiency, flexibility, and biocompatibility, making it particularly suitable for powering human implantable electronic devices.

The ability of some materials to convert mechanical energy (deformations, vibrations, etc.) into electrical energy, or vice versa, is called piezoelectricity, and materials with this property

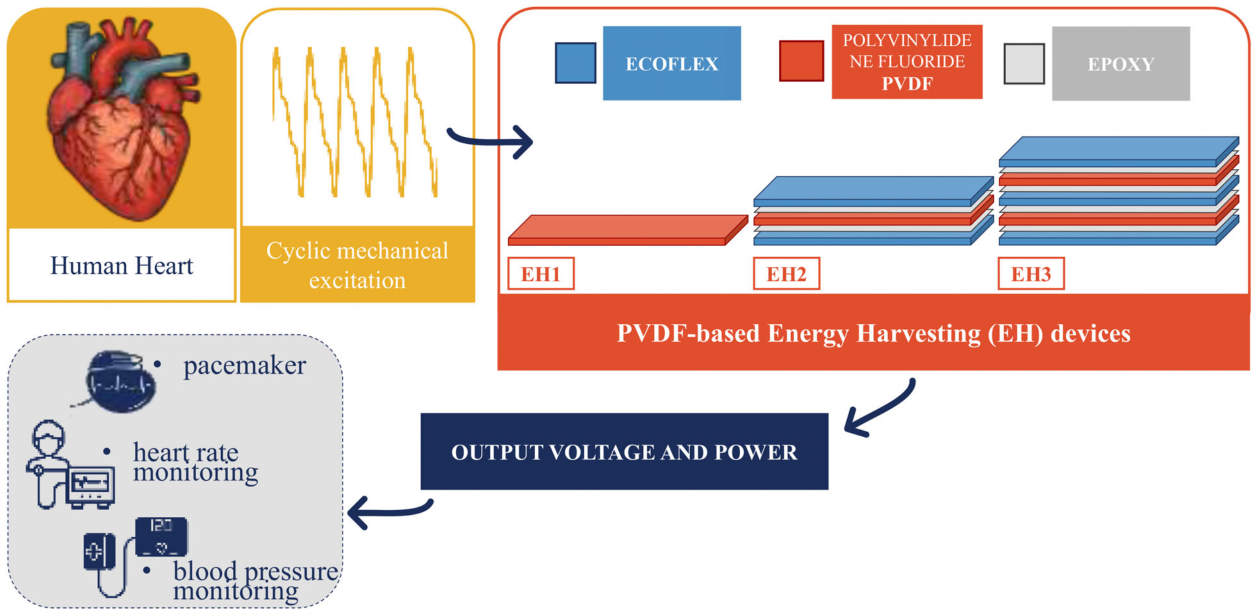

FIGURE 1 | Schematic illustration of the powering process of an implantable electronic device based on EH. In particular, on the right-hand side, the three layouts of the developed EHs are illustrated.

are called piezoelectric materials [2]. Over the past decades, researches have made substantial progress in this field; as an example, self-powered pacemakers based on piezoelectric energy harvesting have been tested in animal models, demonstrating the potential to eliminate the need for battery replacements, thus improving patient welfare [3, 4]. Additionally, piezoelectric energy harvesters have been applied to implantable cardiac sensors, deep brain stimulators, and other devices, enabling real-time monitoring and treatment of physiological conditions [5, 6]. These advancements have laid a solid foundation for the practical application of piezoelectric energy harvesting technology in the biomedical field.

So far, piezoelectric materials developed and used in real applications have been mainly those based on ceramic piezoelectrics, such as the easily available lead zirconate titanate, characterized by a good energy generation performance. However, ceramic-based piezoelectrics are typically brittle and thus cannot undergo large deformations, beyond not being biocompatible because of the presence of unsafe substances for the human body [7–9]. For the above-mentioned reasons, the use of more compliant and lead-free materials is necessary, especially when the energy has to be generated from mechanical deformations induced by movements of the human body.

Polyvinylidene fluoride (PVDF) and its copolymers, i.e. organic semi-crystalline piezoelectric polymers – whose main chemical formula is $(C_2F_2H_2)_n$ – possess excellent piezoelectric properties, high flexibility, strong corrosion resistance, and biocompatibility [10], making them ideal for the development of energy harvesting devices to be used in applications where the interaction with the human body is necessary, such as for supplying energy to implantable electronic devices [11].

Depending on the network chain conformation, PVDF and its copolymers exhibit three primary crystalline phases, namely α, β, and γ. The α-phase is nonpolar, while the γ-phase has a small dipole moment, therefore, no piezoelectric properties are present. The β-phase is the most important one because it provides a strong piezoelectric response [12].

The crystalline β-phase is characterized by aligned molecular dipoles, leading to a non-zero global dipole moment; the process of obtaining the conversion of the α-crystal phase into β-crystal phase is termed *polarization process*, and can be performed by exploiting various technologies such as mechanical stretching [13], electric poling [14], thermal annealing [15, 16], electrospinning [17], etc. It must be recalled that the piezoelectric performance of PVDF is lower than that of traditional piezoelectric ceramics and piezoelectric crystals. Further, it has been discovered that adding nanoparticles into the porous microstructure of PVDF, such as Y-ZnO nanoparticles, enhances the piezoelectric performance [18].

One of the most effective technologies for switching the electric dipole moment in PVDF is represented by the poling technology [14], which is operated through the application of a strong electric field; during the polarization process, domain alignment takes place in the electric field direction, resulting in a high net polarization and in capturing the mobile free charge carriers (oxygen vacancies). For such a purpose, different approaches are available, such as the direct current electric poling (DC poling), the alternating current poling (AC poling), or the corona discharge method [19].

Several studies on energy harvesting making use of piezoelectric-based devices have been conducted in the literature so far. Among them, Almarri et al. [3] reported on piezoelectric energy harvesting and ultralow-power management circuits for medical devices, highlighting the potential of piezoelectric materials in medical applications. Liu et al. [20] reviewed advances in biodegradable piezoelectrics for medical implants, emphasizing the importance of biocompatible piezoelectric materials for implantable devices. Wang et al. [4] developed a wearable multifunctional piezoelectric MEMS device for motion monitoring, health warning, and earphone applications, demonstrating the flexibility and versatility of piezoelectric materials. Nechibvute et al. [5] proposed piezoelectric energy harvesting devices as an alternative energy source for wireless sensors, highlighting their potential in various applications. Pillatsch et al. [6] designed a wireless power transfer system for a human motion energy harvester, combining piezoelectric energy harvesting with wireless power transmission. Khazaee et al. [21] explored contact-based impact energy harvesting from ultralow-frequency intracardiac kinetic energy, targeting the specific energy source of heartbeats. Guan et al. [22] developed a self-powered wearable piezoelectric nanogenerator for physiological monitoring based on lead zirconate titanate/microfibrillated cellulose@polyvinyl alcohol (PZT/MFC@PVA) composites, expanding the classical application scope of piezoelectric materials in wearable devices. In [23], Tsukamoto et al. developed bimorph piezoelectric vibration energy harvesters with flexible 3D meshed-core structures for low-frequency vibrations, addressing the challenges of low-frequency energy harvesting. High-performance flexible piezoelectric nanogenerators with folded structures based on CNTs-modified BCβZT/P(VDF-HFP) composite films have been developed by Wang et al. [9], advancing the development of flexible piezoelectric devices. Shi et al. [24] developed MEMS-based broadband piezoelectric ultrasonic energy harvesters for enabling self-powered implantable biomedical devices, addressing the energy harvesting needs of implantable devices. Mokhtari et al. [25] created self-powered nanostructured piezoelectric filaments as advanced transducers for new cochlear implants, expanding the application scope of piezoelectric materials in biomedical fields. Flexible and lead-free piezoelectric nanogenerators based on electrospun BZT-BCT/P(VDF-TrFE) nanofibers used as self-powered sensors, addressing the environmental concerns of traditional piezoelectric materials, have been developed by Liu et al. [26]. Pal et al. [27] enhanced the energy storage and piezoelectric performance of three-phase (PZT/MWCNT/PVDF) composites, advancing the development of composite piezoelectric materials. Zheng et al. [28] presented the first in vivo demonstration of a breathing-driven triboelectric nanogenerator (TENG) designed to power a cardiac pacemaker, thus eliminating the need for invasive battery replacements; the developed TENG harvests energy from respiratory motion and generates a stable electrical output ranging from 3 to 5 $\mu W/cm^2$, which is sufficient to sustain the operation of a pacemaker indefinitely. Dagdeviren et al. [29] introduced a conformal piezoelectric energy harvesting system that captures kinetic energy from the heart, lung breathing, and diaphragm motions to power implantable medical devices. Hu et al. [30] successfully developed a conformal piezoelectric device made up of PVDF film encapsulated in a PDMS substrate; the energy harvesting device, undergoing a 9.1 mm tip displacement, provided a power output of 1 µW and a voltage output of $\pm$ 1.4 V during each cycle. The study by Lu et al. [31] demonstrated that an ultra-flexible PZT-based piezoelectric device integrated with the heart generates peak-to-peak voltages of up to 3 V from myocardial contractions, thus effectively harvesting biomechanical energy to supply the required power to implantable medical devices. Li et al. [32] demonstrated a successful long-term in vivo operation of cardiac nanogenerators in swine, achieving sustained energy harvesting from heartbeats for over 6 months without degradation in output or adverse tissue reactions; the developed nanogenerators produced 5–8 $\mu W/cm^2$, a sufficient energy to power pacemakers continuously, thus providing a critical milestone toward eliminating surgical battery replacements in cardiac devices. Dong et al. [33] developed a helical-designed porous PVDF-TrFE energy harvesting device integrated with an existing pacemaker; the helical configuration of the energy harvesting device demonstrated significant advantages in capturing both complex vibrational motion and the bending/twisting of the lead caused by the beating heart. Both in vitro and in vivo results showed that the energy harvesting device can effectively generate substantial electrical energy directly from the motion of a pacemaker lead. Microporous P(VDF-TrFE)/PDMS composite films have been developed by Xu et al. [34] to harvest energy from cardiac motion; by mixing 30% ZnO with 0.1% multiwall carbon nanotubes (MWCNTs), an output of 3.22 ± 0.24 V has been achieved, a voltage output about 46 times higher than that of pure P(VDF-TrFE) films.

In this study, we present a novel multilayer flexible energy harvester (FEH) utilizing polyvinylidene fluoride (PVDF) piezoelectric polymer layers, integrated between dielectric elastomer substrates made of silicone Ecoflex 00–30, a highly versatile and biocompatible polymer widely used in medical devices due to its nontoxic, non-allergenic, and, in some conditions, antimicrobial properties [35].

Three distinct device configurations – namely PVDF (1-layer, EH1), Ecoflex/PVDF/ Ecoflex (3-layers, EH2), and Ecoflex/PVDF/Ecoflex/PVDF/Ecoflex (5 layers, EH3) – are systematically tested to quantify the energy harvesting performance. An experimental framework is employed to characterize the devices under mechanical deformation. Key metrics, including output voltage, capacitance, and impedance, are measured to assess the electrical properties of each configuration. Further, we simulate the use of the developed EH devices in applications where the mechanical energy is provided by the heart motion. Starting from real heart kinematic data, we use the beam's large deflection theory, characterized by small strains and moderate-to-large rotations hypotheses, to determine the electric potential arising in the EH device. The proposed integrated experimental-simulation approach aims to advance the design of flexible, wearable energy harvesting systems for applications involving low-frequency mechanical excitation.

2 | Piezoelectricity in Polymeric Materials

The constitutive relationships of a piezoelectric material – written in the stress-charge form in the current configuration ($\boldsymbol{\sigma}, \boldsymbol{D} \leftarrow \boldsymbol{\varepsilon}, \boldsymbol{E}$) – are given by:

$$\begin{aligned} \boldsymbol{\sigma} &= \boldsymbol{\sigma}_M + \boldsymbol{\sigma}_p = \boldsymbol{C}\,\boldsymbol{\varepsilon} - \boldsymbol{e}^T \boldsymbol{E} \\ \boldsymbol{D} &= \boldsymbol{e}\,\boldsymbol{\varepsilon} + \boldsymbol{\epsilon}\,\boldsymbol{E} \end{aligned} \tag{1}$$

where $\boldsymbol{\sigma}_M$ is the mechanical and $\boldsymbol{\sigma}_p$ are the piezoelectric Cauchy stress tensors, respectively, $\boldsymbol{C}$ is the fourth-order elasticity tensor, $\boldsymbol{e}$ is the third-order piezoelectric constant tensor (in stress-charge form, with units: [charge · surface area^{-1}]), $\boldsymbol{E}$ is the electric field, while $\boldsymbol{\epsilon} = \epsilon_r \boldsymbol{\epsilon}_0$ is the second-order dielectric constant tensor (units: [Farad · length^{-1}], with ϵ_0 the vacuum dielectric constant tensor, and ϵ_r the relative permittivity), and $\boldsymbol{\varepsilon} = \nabla \boldsymbol{u}$ is the strain tensor [36]. The polarization $\mathbb{p}$ arising in a piezoelectric material is usually assumed to be linearly dependent on the mechanical deformation (or the mechanical stress) through the piezoelectric tensors $\boldsymbol{e}$ (or the piezoelectric tensors $\boldsymbol{d}$) as:

$$\mathbb{p} = \boldsymbol{e}\,\boldsymbol{\varepsilon} = \boldsymbol{e}\,\boldsymbol{C}^{-1}\,\boldsymbol{\sigma}_M = \boldsymbol{d}\,\boldsymbol{\sigma}_M \tag{2}$$

The governing equations of the coupled mechanical and electric field (i.e., the equilibrium equations and Gauss' law) involving the mechanical displacement field vector $\boldsymbol{u}$ and the electric potential Φ are [36]:

$$\begin{aligned} &\underbrace{\nabla\cdot(\boldsymbol{C}\,\nabla\boldsymbol{u})}_{\nabla\cdot\boldsymbol{\sigma}_M} + \underbrace{\nabla\cdot\left(\boldsymbol{e}^T\nabla\Phi\right)}_{\nabla\cdot\boldsymbol{\sigma}_E} + \rho\,\boldsymbol{b} = 0 \quad \text{in} \quad B \\ &\nabla\cdot\boldsymbol{D} = \nabla\cdot(\boldsymbol{e}\,\nabla\boldsymbol{u}) - \nabla\cdot\,(\epsilon\,\nabla\Phi) = 0 \quad \text{in} \quad B \end{aligned} \tag{3}$$

with the corresponding boundary conditions (BCs):

$$\begin{aligned} &\boldsymbol{u} = \overline{\boldsymbol{u}} && \text{on } \partial B_u && \text{(Displacement BC)} \\ &\sigma\cdot\boldsymbol{n} = \bar{\boldsymbol{t}} && \text{on } \partial B_t && \text{(Traction BC)} \\ &[\boldsymbol{D}]\cdot\boldsymbol{n} = q_S && \text{on } \partial B_E && \text{(Electric displacement BC)} \\ &\Phi = \overline{\Phi} && \text{on } \partial B_\Phi && \text{(Electric potential BC)} \end{aligned} \tag{4}$$

Using the Voigt notation for expressing tensors and vectors in a 3D setting, the piezoelectric tensor $\boldsymbol{d}$ (or $\boldsymbol{e}$) is represented by a 3×6 matrix, and the dielectric tensor ε by a 3×3 matrix. In particular, assuming the material to be mechanically and electrically transversally isotropic (with z being the main polarization direction), in matrix forms the above-mentioned tensors are represented (typical of PVDF piezoelectric polymer) as follows:

$$\boldsymbol{d}_{3\times6} = \begin{bmatrix} 0 & 0 & 0 & 0 & d_{15} & 0 \\ 0 & 0 & 0 & d_{24} & 0 & 0 \\ d_{31} & d_{32} & d_{33} & 0 & 0 & 0 \end{bmatrix}, \quad \epsilon_{3\times3} = \begin{bmatrix} \epsilon_{11} & 0 & 0 \\ 0 & \epsilon_{22} & 0 \\ 0 & 0 & \epsilon_{33} \end{bmatrix} \tag{5}$$

being d_{33} the main piezoelectric constant, while ε_{33} is the dielectric constant in the $z-$direction. The remaining parameters ($d_{31} = d_{32}$, $d_{24} = d_{15}$, $\varepsilon_{11} = \varepsilon_{22}$) are the corresponding constants referred to the coupling between the direction 3 (z) and the directions 1 (x) and 2 (y).

In a polarizable piezoelectric material having an initial permanent polarization $\mathbb{p}_p$ (existing in the absence of any external electric field), the electric displacements in the strain form simplifies to:

$$\boldsymbol{D} = \boldsymbol{e}\,\boldsymbol{\varepsilon} + \mathbb{p}_p + \varepsilon\,\mathbf{E} \tag{6}$$

Accordingly, the Maxwell Cauchy stress tensor becomes:

$$\begin{aligned} \boldsymbol{\sigma}_E = \epsilon\,\mathbf{E}\otimes\boldsymbol{E} &+ \frac{1}{2}\left[\mathbb{p}_p\otimes\boldsymbol{E} + \left(\mathbb{p}_p\otimes\boldsymbol{E}\right)^T\right] \\ &+ \frac{1}{2}\left[\boldsymbol{e}\,\boldsymbol{\varepsilon}\otimes\boldsymbol{E} + (\boldsymbol{e}\,\boldsymbol{\varepsilon}\otimes\boldsymbol{E})^T\right] \\ &+ -\frac{1}{2}\left[\varepsilon\,\mathbf{E}\cdot\boldsymbol{E} + \mathbb{p}_p\cdot\boldsymbol{E} + \boldsymbol{e}\,\boldsymbol{\varepsilon}\cdot\boldsymbol{E}\right]\mathbf{1} \end{aligned} \tag{7}$$

If the dielectric end piezoelectric properties are homogeneous and the permanent polarization $\mathbb{p}_p$ is absent throughout the medium, using Gauss' law for a charge-free problem ($\nabla\cdot\boldsymbol{D} = 0$), the electric potential Φ arising in a mechanically deformed piezoelectric material can be obtained by solving Poisson's equation whose unknown variable is the electric potential Φ:

$$\boldsymbol{d}\,\nabla\cdot\boldsymbol{\sigma} - \epsilon\,\nabla\cdot\,(\nabla\Phi) = 0 \tag{8}$$

with electric boundary conditions:

$$\begin{aligned} \Phi = \bar{\Phi} \quad &\text{on} \quad \partial B_\Phi \\ \boldsymbol{D}\cdot\boldsymbol{n} = q_S \quad &\text{on} \quad \partial B_E \end{aligned} \tag{9}$$

For an electrically orthotropic material in a simple 2D framework, the problem is described by the following equation:

$$\begin{aligned} \nabla\cdot\boldsymbol{d}\,\boldsymbol{\sigma} = \epsilon_0\left(\varepsilon_{rx}\frac{\partial^2\Phi}{\partial x^2} + \varepsilon_{ry}\frac{\partial^2\Phi}{\partial y^2}\right) = \left(d_{12}\frac{\partial\tau_{xy}}{\partial x}\right) \\ + \left(d_{21}\frac{\partial\sigma_x}{\partial y} + d_{22}\frac{\partial\sigma_y}{\partial y}\right) \end{aligned} \tag{10}$$

The solution of a piezoelectric problem consists of finding the electric potential difference Φ arising between the two electrodes.

3 | Materials and Methods

3.1 | Materials and Preparation of the PVDF Multilayer EH Devices

Piezoelectric PVDF sheets with flexible CuNi electrodes were purchased from PolyK Technologies, LLC (State College, PA16803 USA). Ecoflex (00-30), purchased from Smooth-On, Inc., is used as a dielectric interlayer. To create our Ecoflex 00–30 film, we employ the precise doctor-blade coating method [37], ensuring a high-quality product. Ecoflex 00–30 was chosen as the encapsulation material because of its outstanding flexibility and biocompatibility, which are essential for both wearable and implantable applications. Its low viscosity and high stretchability allow for smooth integration with soft substrates while preserving structural integrity during repeated deformations.

The preparation of the energy harvesting devices begins with manually cutting rectangular sheets of polyvinylidene fluoride PVDF-CuNi-P0110 with sprayed 80 nm thick CuNi electrode. The piezoelectric PVDF sheet is then embedded in Ecoflex 00–30 layers by using an epoxy resin. Finally, copper–nickel (CuNi) electrodes, with 80 nm thickness, are connected to the top and bottom surfaces of the sandwiched PVDF layer. In devices with two PVDF layers, the piezoelectric sheets are connected electrically in parallel. The main geometrical, mechanical, dielectric, and piezoelectric parameters of the materials used are listed in Table 1. In particular, the epoxy resin thickness is negligible with respect to that of the PVDF and of the dielectric layer, so it does not influence significantly the energy performance of the EH. The dielectric to PVDF layers thickness ratio has been assumed to be equal to about 6.

TABLE 1 | Main geometrical, physical, and mechanical parameters of the used materials.

Parameter Material	Size [mm]	Thickness w_i [µm]	Young's modulus E [MPa]	Relative permittivity ε_r [–]	Piezoelectric coefficient d_{33} [pC/N]	Piezoelectric coefficient d_{31} [pC/N]
PVDF	30 × 6	110	2500	∼ 12.5	∼ 30	∼ 30
Epoxy resin	30 × 6	∼ 20	—	∼ 3.5	—	—
Ecoflex 00–30	30 × 6	640	∼ 0.04	∼ 2.8	—	—

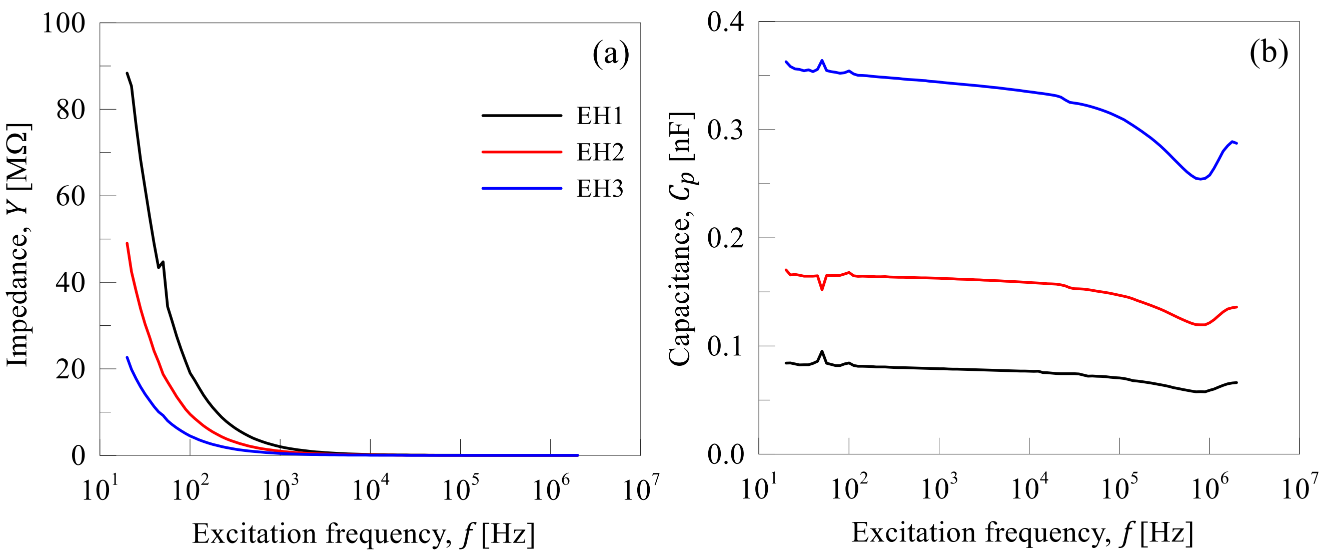

FIGURE 2 | Impedance (a) and capacitance (b) of the three PVDF-based energy harvester devices EH1, EH2, and EH3.

3.2 | Electrical Measurements

The capacitance and impedance versus frequency have been experimentally measured by using an E4980A Precision LCR Meter, which operates at frequencies between 20 Hz and 1 MHz, as shown in Figure 2. When subjected to an excitation with a frequency ranging in the interval 20 Hz to 1 MHz, the capacitance of EH1, EH2, and EH3 devices falls within the ranges: 0.0589 nF to 0.087 nF, 0.12 nF to 0.17 nF, and 0.36 nF to 0.25 nF, respectively.

According to the parallel-plate capacitor formula, theoretically an increase in the thickness should lead to a decrease in the capacitance. However, our experimental results reveal a twofold increase in capacitance for the multilayer Ecoflex 00–30/PVDF/Ecoflex 00–30 structure (EH2) compared to the pure PVDF film (EH1) (see Figure 2). This increase can be explained by the interfaces introduced between the PVDF and Ecoflex layers [38]. The mismatches in permittivity and conductivity between these materials lead to interfacial polarization (the Maxwell–Wagner–Sillars effect [39]). As a result, charges accumulate at the interfaces, enhancing the overall dielectric response, particularly at lower frequencies. This additional interfacial polarization explains why the measured capacitance is higher than what would be predicted by a simple series model. Thus, the encapsulation effectively generates new interfacial regions, which play a significant role in boosting the system's total polarization and capacitance.

When comparing energy harvesting devices with a single layer to those featuring two active PVDF films, the dual-layer energy harvester demonstrates improved performance. Specifically, at 20 Hz excitation, it shows an increase in capacitance by a factor of 2.13 and a reduction in impedance by a factor of 1.8. This behavior can be attributed to the parallel connection of the PVDF layers, which enhances capacitance and reduces impedance, ultimately improving the electrical performance of the device [40].

It is worth mentioning that the high internal electrical resistance (R_{int}) of the PVDF material decreases the output voltage and efficiency, requiring careful load optimization and circuit design [41]. According to the maximum power transfer theorem, to achieve maximum power transfer at the output, the external load resistance must equal the internal resistance of the device. In this study, the output power, current, and voltage were predicted theoretically across a broad range of load resistance values [42].

4 | Evaluation of the EH Electrical Output

The high internal impedance of polyvinylidene fluoride (PVDF) material [43] – an electrical property that opposes current flow – decreases the output voltage and efficiency, requiring careful load optimization and circuit design. For low-frequency applications (with f ranging from 1 to 6 Hz), the alternating current (AC) impedance (i.e., the capacitive reactance) is the dominant factor in determining the internal resistance R_{int} of a piezoelectric PVDF material; in an EH device, the internal resistance corresponds to the capacitive reactance (X_C) that can be written as follows [44]:

$$X_C = \frac{1}{2\pi f C_p} = \frac{1}{\omega\, C_p} \tag{11}$$

where the capacitance C_p of a parallel plate capacitor, with isotropic electric properties, is given by $C_p = (\epsilon_r \epsilon_0 A_c)/s$, being A_c, $\epsilon_0 = 8.854 \cdot 10^{-12}$ F/m, ϵ_r, s the area, the vacuum permittivity, the relative permittivity, and the thickness of the piezoelectric layer, respectively. For the PVDF layer here adopted, the capacitive reactance results to be: $X_C = 879$ MΩ at 1 Hz, $X_C = 439$ MΩ at 2 Hz, and $X_C = 293$ MΩ at 3 Hz.

In a 2D reference system $x - y$, upon the application of mechanical stresses σ_x, σ_y the open-circuit voltage Φ_{oc} generated at the surface of the piezoelectric material can be calculated as [45]:

$$\Phi_{oc} = \frac{\sigma_x\, d_{21} + \sigma_y d_{22}}{\epsilon_r\, \epsilon_0}\, w_{PVDF} \tag{12}$$

For the problem under study, $\sigma_y \cong 0$, i.e., the transversal stress component acting on the piezoelectric layers is absent, thus providing $\Phi_{oc} \cong \frac{\sigma_x\, d_{21}}{\epsilon_r\, \epsilon_0}\, w_{PVDF}$.

The electrical model of a piezoelectric harvester is typically represented by a current source in parallel with the internal impedance of the piezoelectric element. For analytical purposes, hereafter the piezoelectric is modeled using its Thevenin equivalent, i.e. a sinusoidal voltage source in series with the complex impedance of the harvester. The Thevenin-based formulation is widely adopted because it simplifies system-level analysis and enables impedance-matching strategies to maximize power transfer; it also provides a clear pathway to optimize load resistance and interface circuitry for energy harvesting applications.

The internal impedance consists primarily of the piezoelectric capacitance C_p connected in parallel with internal resistance. Based on the general relationship existing between voltage, frequency, and load resistance R_L of an external circuit connected to the EH device, the voltage obtainable is expressed as [46]:

$$\Phi_c = \Phi_{oc} \frac{R_L}{|Z| + R_L} \tag{13}$$

where the total complex device impedance Z is the reciprocal of the total admittance Y, the latter –for two impedances in parallel – being the sum of individual admittances, $Y = Y_{int} + Y_{C_p}$, i.e.:

$$Z = \frac{1}{Y} = R_{int} - j\frac{1}{\omega\, C_p} \tag{14}$$

being j the imaginary unit, and $|Z| = |R_{int} - j\, X_c| = \sqrt{R_{int}^2 + 1/(\omega\, C_p)^2}$ is its modulus. The internal resistance of the piezoelectric plate can be evaluated as: $R_{int} = \frac{1}{Q_m\, \omega\, C_p} = \frac{X_c}{Q_m}$, where Q_m is the so-called mechanical quality factor (assuming values in the range 2–20 for PVDF) measuring the mechanical energy loss in the piezoelectric material [47]. For the PVDF elements whose characteristics are given in Table 1, the internal resistance, assuming a mechanical quality factor $Q_m = 17$ results to be $R_{int} = 51.7$ MΩ, 25.8 MΩ, 17.2 MΩ for $f = 1$, 2, 3 Hz, respectively. The open circuit voltage Φ_{oc} represents the maximum value of the voltage generated by a piezoelectric device when no external circuit is connected to it (i.e. $\Phi_c = \Phi_{oc}$, $R_L \rightarrow \infty$), while $\Phi_c < \Phi_{oc}$ when an external circuit with finite resistance is connected to the EH. Finally, it is worth mentioning that the power generated by the EH device connected to a circuit is given by $P = \frac{\Phi_{oc}^2}{(|Z|+R_L)^2} R_L$ and, according to the maximum power transfer theorem (which states that the power delivered to an external load is maximized when the load resistance equals the internal impedance of the source), the external load resistance must equal the internal resistance of the device, $R_L = |Z|$, i.e. $P_{max} = \frac{\Phi_{oc}^2}{4R_{int}}$.

When the EH is connected to an external load resistance R_L, the voltage and the current flowing in the circuit decay exponentially as: $\Phi\ (t) = \Phi_c\ e^{-t/(R'\ C_p)}$, $I\ (t) = (\Phi_c/R_L)\ e^{-t/(R' C_p)}$, being $R' = (1/|Z|\ + 1/R_L)^{-1}$ the equivalent resistance of both the external circuit and of the piezoelectric film's internal resistance. The instantaneous power and the total energy provided to the system by the EH are given by:

$$P\,(t) = \left(\Phi_c^2/R'\right)\ e^{-2t/\left(R'\ C_p\right)}, \qquad E_n = \int_{t=0}^{T} P\,(t)\, dt = \frac{1}{2}\, C_p \Phi_c^2 \tag{15}$$

respectively, where the time period T of the mechanical stress cyclically applied to the EH is assumed to be large enough compared to the characteristic decaying time of the system.

Based on the above expressions and assuming the PVDF to be stressed under uniform tension of $\sigma_x = 0.1$ MPa, the voltage, the current, and the power produced by EH2 and EH3 for different load resistances and frequency excitations have been obtained, as shown in Figure 3. An output voltage Φ_c of about 1.68 V, an output current of about 7 nA, and a maximum power of about 0.007 μW can be achieved for the EH2 for a load resistance of 380 MΩ at $f =$ 3 Hz, while for the same excitation frequency an output voltage Φ_c of about 1.51 V, an output current of about 23 nA, and a power of about 0.015 μW can be achieved for a load resistance of 150 MΩ for EH3. It is worth mentioning that the order of magnitude of the obtained output voltage and current makes them suitable for diverse biomedical applications, such as heart monitoring [31].

5 | Mechanical Model of the EH Flexible Device

The considered EH device can be conveniently modeled as a thin beam undergoing large displacements. Within this context, we adopt the limited rotations theory, according to which $\varepsilon \ll 1$ and moderate to large rotations are assumed. The beam's centerline point positions in the undeformed configuration and the deformed centerline of the beam are expressed as [48, 49]:

$$\begin{gathered} \boldsymbol{r}_0\ (s) = s\, \boldsymbol{i}, \qquad 0 \le s \equiv x \le L \\ \boldsymbol{r}\ (s) = \boldsymbol{r}_0\ (s) + u\,(s)\ \boldsymbol{i} + v\,(s)\ \boldsymbol{j}\ = x\,(s)\ \boldsymbol{i} + v\,(s)\ \boldsymbol{j}, \qquad 0 \le s \le L \end{gathered} \tag{16}$$

being s the curvilinear abscissa of the beam.

We assume the centerline of the beam to be axially undeformable, and to possess an initial non-straight configuration quantified by

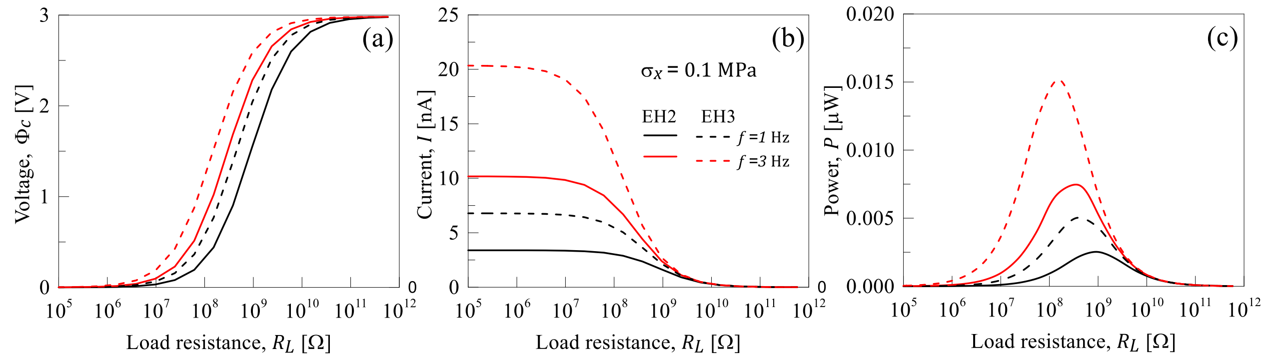

FIGURE 3 | Predicted output voltage (a), current (b), and power (c) vs load resistance for EH2 and EH3 stressed with $\sigma_x = 0.1$ MPa for two different excitation frequencies of the device.

an initial small imperfection $v_0\ (s) = a \sin \frac{\pi\, s}{L}$ (or equivalently $\theta_0(s) = v_0'\ (s)$) providing the initial curvature $\kappa_0(s) \cong v_0''\ (s) = \theta_0'\ (s) = -a\left(\frac{\pi}{L}\right)^2 \sin \frac{\pi\, s}{L}$; due to the above hypothesis, the problem has a purely geometrical nature. By using the beam's centerline slope $\theta(s)$ to describe its deformed shape, we have $x'\ (s) = \cos\ \theta(s)$, $v'\ (s) = \sin\ \theta(s)$.

The inextensibility hypothesis requires satisfying the following constraint:

$$\sqrt{x'^2\,(s) + v'^2\,(s)} = 1 \qquad 0 \leq s \leq L \tag{17}$$

Let's assume that the beam representing the EH device undergoes an axial displacement u_c at one of its extremities while the other is fixed, thus:

$$x\,(s = L) - x\ \ (s = 0) = L -\ u_c = \int_0^L \cos\theta\,(s)\,ds \tag{18}$$

The variational formulation of the problem requires the first variation of the following functional $\mathcal{L}$ to vanish.

$$\mathcal{L}\ (\theta, N) = \frac{\bar{E}\bar{I}}{2}\ \int_0^L \left[\theta'\,(s) - \theta_0'\,(s)\right]^2 ds + N\left[\int_0^L \cos\theta\,(s)\,ds - (L - u_c)\right] \tag{19}$$

where $\bar{E} = \int_A E(y)\,dA\,/A$ is the average Young's modulus of the cross section of the beam, while $\bar{I} = \int_A E(y)\,y^2\,dA\,/\bar{E}$ is the weighted average moment of inertia of the beam's cross section, and N is the axial force, here assuming the role of a Lagrange multiplier ensuring the beams inextensibility; the above average quantities are necessary when the cross section of the beam is not homogeneous, but it is made of layers of different materials like in the case we are considering here.

$$\begin{aligned}\delta\mathcal{L}\ (\theta, N) = B.T. - \int_0^L\ \left[\bar{E}\bar{I}\,\left(\theta'' - \theta_0''\right) + N\sin\theta\right]\ \delta\theta\ ds \\ +\,\delta N\ \int_0^L\left[\cos\theta - (L - u_c)\right]ds = 0\end{aligned} \tag{20}$$

being $B.T. = \left[\bar{E}\bar{I}(\theta' - \theta_0')\delta\theta\right]_0^L$ the boundary term; Euler's equation results to be: $\bar{E}\bar{I}(\theta'' - \theta_0'') + N\ \sin\theta = 0,\ 0 \leq s \leq L$. Assuming the beam to be simply supported with a roller at one extremity, the deformed shape results to be given by the following equations:

$$x\ (s) = x\,(0) + \int_0^s \cos\theta\,(\xi)\,d\xi, \qquad v\ (s) = v\,(0) + \int_0^s \sin\theta\,(\xi)\,d\xi \tag{21}$$

If the initial imperfection is small, i.e., $a \ll L$, the deformed shape of the beam can be expressed in the form (first mode) $\theta\ (s) = \Xi\ \cos\frac{\pi\, s}{L}$, where Ξ can be determined from the known axial displacement u_c:

$$L -\ u_c = \int_0^s \cos\left(\Xi\ \cos\frac{\pi\, s}{L}\right) ds \tag{22}$$

leading to:

$$L -\ u_c = \frac{L}{\pi}\ \int_0^s \cos\left(\Xi\ \cos\varphi\right) d\varphi = L\,J_0\,(\Xi) \tag{23}$$

where $J_0(\Xi)$ is the zero-order Bessel function. If u_c/L is small, $J_0(\Xi) \cong 1 - \Xi^2/4$ and thus Ξ results to be $\Xi \cong 2\sqrt{u_c/L}$. In parametric form, the equations describing the deformed shape of the beam's centerline are:

$$\begin{aligned}x\ (s) &= \frac{L}{\pi}\ \int_0^{\pi s/L} \cos\left(\Xi\ \cos\varphi\right) d\varphi \\ v\ (s) &= \frac{L}{\pi}\ \int_0^{\pi s/L} \sin\left(\Xi\ \cos\varphi\right) d\varphi,\end{aligned} \tag{24}$$

In line with the limited rotations theory, the longitudinal strain taking place at a generic point – identified by the local coordinates (s, y) – is approximately expressed by:

$$\varepsilon\,(s, y) \cong -y\ v''\,(s) \qquad 0 \leq s \leq L \tag{25}$$

The solution of the above integrals is obtained numerically by considering the boundary conditions corresponding to the longitudinal relative displacements of the EH device (point C, see Figure 4), while the transversal displacement of point C is always assumed to be zero, i.e. $v_c = 0$.

The above illustrated model enables us to estimate the energy production of a beam-like EH device made of PVDF layers; in particular, we simulate the output provided by EH3 when a periodic axial displacement u_c is applied at a frequency f by assuming an initial imperfection $a\ =\ 2 \cdot 10^{-4}$ m (it can be easily shown that the deformed shape of the beam upon applying the axial displacement, does not depend significantly on a). The

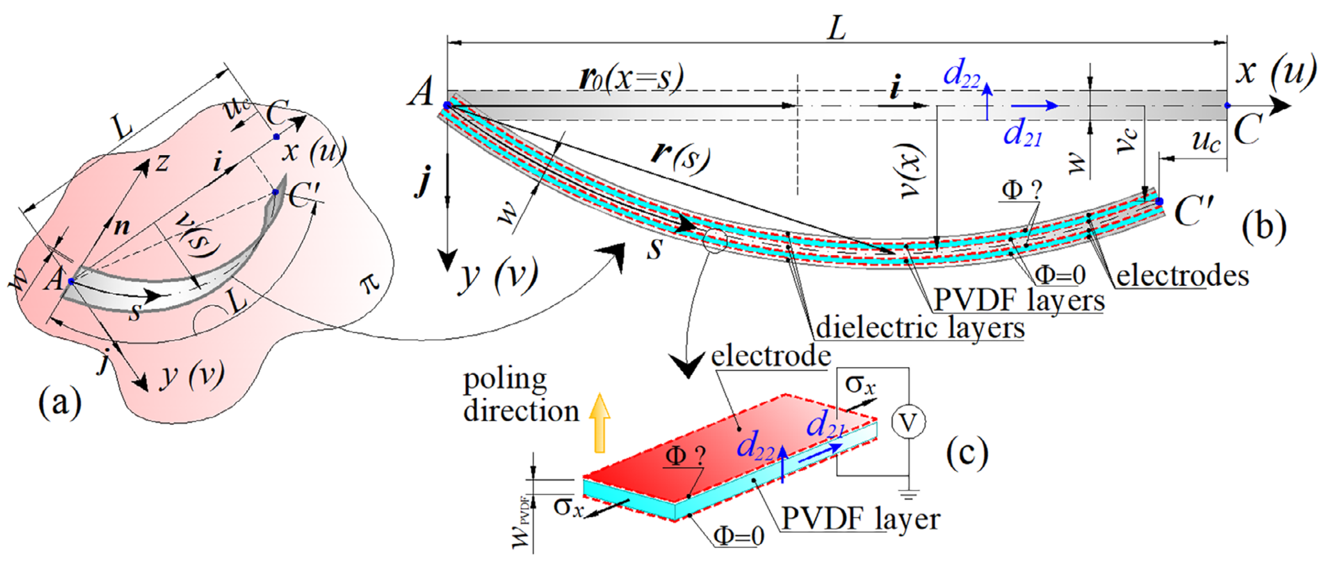

FIGURE 4 | Schematic of the local reference system (a) adopted for measuring the relative axial and transversal displacements of the three points along the EH beam device. Kinematic quantities on the π (x − y) plane (b) and schematic representation of a piezoelectric layer with a d_{21}-coupling mode (c).

open-circuit voltage Φ_{oc} and the voltage Φ_c (evaluated for a load resistance equal to $R_L = 1\,\mathrm{M\Omega}$) are determined, as well as the power P and the energy E_n produced in one cycle. According to the model, EH1 and EH2 do not produce energy since the deformation of the midsurface of the layered beam is zero. Since for the multilayer EH3 the deformation of the PVDF layers is not uniform along the beam, its average value is used to determine the stress state.

In Figure 5, the simulation results are shown for different axial displacements applied to the beam EH3; the comparison with experimental measurements of EH3 is also reported for the case $u_c/L = 0.067$, which shows a reasonable agreement with the model outcomes.

In Figure 6 the complete experimental results expressed in term of voltage for EH1, EH2, and EH3 are reported *vs* the excitation frequency ranging between 1 to 8 Hz; it must be noted that a non-zero output voltage is obtained also for EH1 and EH2 having a single piezoelectric layer lying on the midsurface of the beam for which the theoretical model predicts zero strain and so no voltage. However, the cyclic displacements applied in the experimental tests produce an axial stretch in the PVDF layer because of the constraints applied at the extremities of the EH beams, which do not allow for complete horizontal free movements. EH2 shows an improvement with respect to EH1 in terms of voltage, due to the presence of the two dielectric layers containing the piezoelectric one.

It is worth recalling that the application of EH in real applications requires the device to be able to withstand a high number (of the order of $1 \div 4 \cdot 10^8$) of repeated loading cycles. PVDF membranes exhibit a good mechanical fatigue resistance against both tension and compression, making them suitable for applications like flexible energy harvesters and sensors that require long-term durability. As a matter of fact, PVDF can safely bear millions of deformation cycles without significant loss of mechanical performance and stable voltage output, although the fatigue behavior depends on the strain levels applied and environmental conditions [50, 51].

6 | Energy Harvesting from the Heart Motion

6.1 | Kinematic of the Heart Motion

Data related to the spatio-temporal motion of the Left Ventricle (LV) recorded from human patients have been used for the simulations considered in the present section.

All the data were acquired by 3D-STE with a PST-D25SX Aplio-Artida ultra-sound system (Toshiba Medical Systems Co, Tokyo, Japan); at the time of data acquisition, this ultrasound machine was housed in the Dept. of Cardiovascular, Respiratory, Nephrological, Anesthesiological and Geriatric Sciences at the University Hospital Umberto I, Sapienza, and Univ. of Rome, Italy. The study was performed under the approval of the review board of the host department, and in accordance with the ethical guidelines of the Declaration of Helsinki. Written informed consent was obtained from all participants.

Data acquisition was performed using an unlocked version of the software installed on the 3D-STE Aplio-Artida, which gives access to the raw data with the position of all the landmarks tracked in the video recording. The unlocked software is part of a research collaboration among the host department and Toshiba Medical System Europe.

The echocardiographic discretization of a heart chamber surfaces (endocardial or epicardial) results in a cloud of 1297 points for each surface. These data points correspond to the segmentation of the LV in 36 planes along the axial direction (base to apex), where each plane is equally divided into 36 sections along the hoop direction plus one point at the apex. Then, at each time

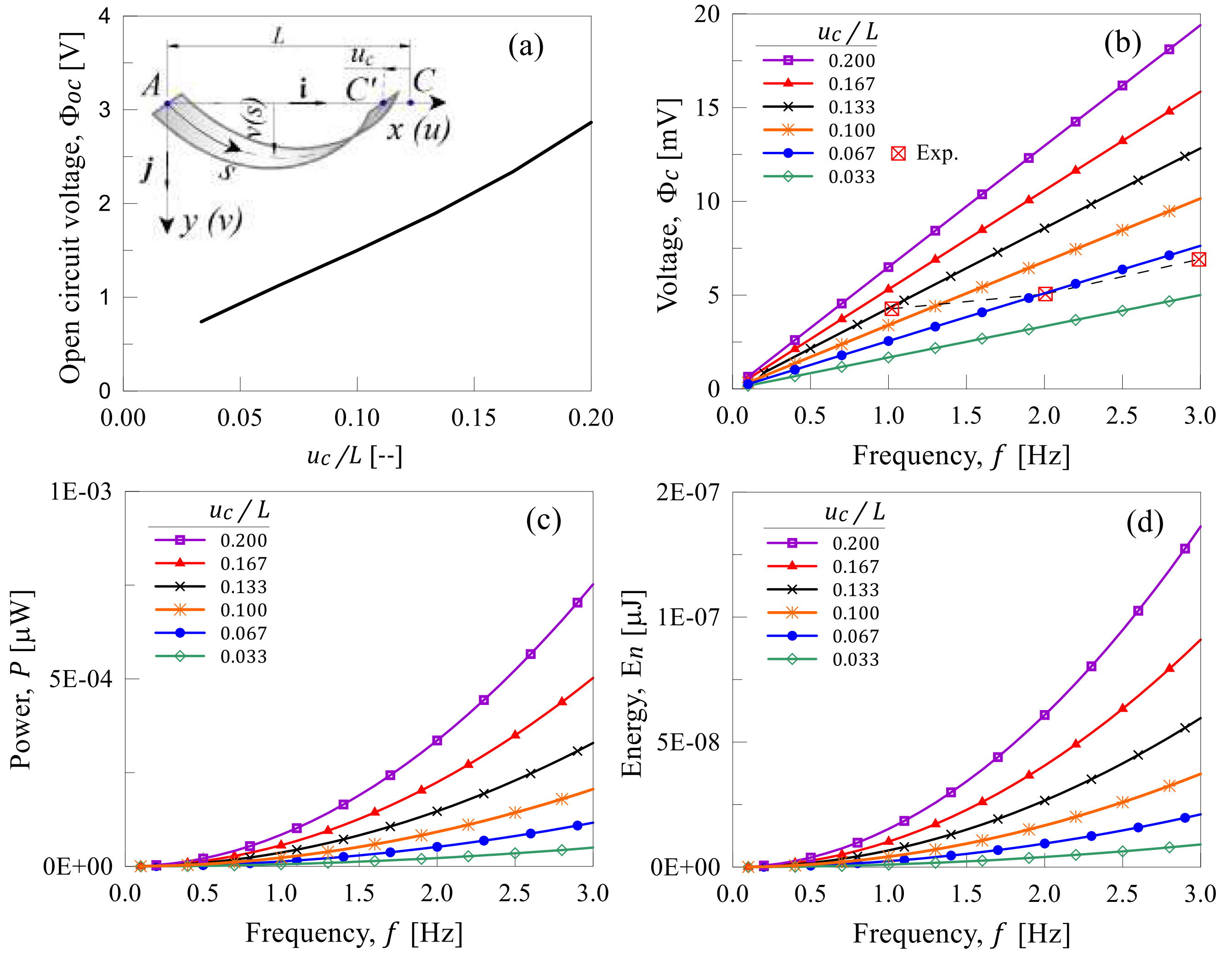

FIGURE 5 | Output in terms of open-circuit voltage Φ_{oc} (a), voltage Φ_c (b), power P (c) and energy E_n per cycle (d) for the EH3 under various longitudinal displacements u_c and excitation frequencies f. An electrical load resistance $R_L = 1\ M\Omega$ (a typical value for oscilloscopes) is assumed.

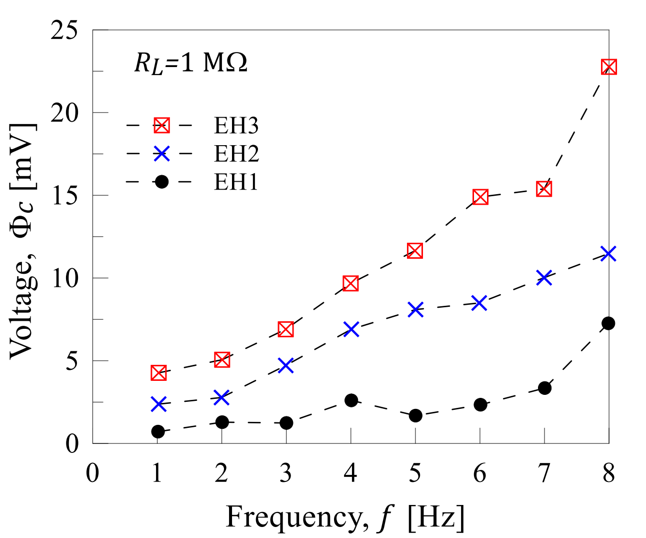

FIGURE 6 | Experimental results expressed in terms of voltage Φ_c for the EH1, EH2, and EH3 under an axial displacement $u_c = 2.2$ mm and various excitation frequencies f. The electrical load resistance of the used oscilloscope is equal to $R_L = 1\ M\Omega$.

frame $j = 1, 2, \ldots, n$, with $j = 1$ corresponding to the end diastolic state, and n depending of the beating pace of each subject (usually $n \sim 20$), we have a set of points p_i with $i = (36 \times 36 + 1) \times 2$, describing the configuration of the two LV surfaces along the cardiac cycle. The coordinates refer to an orthogonal system (i_1,i_2,i_3) where i_3 defines the axial direction and i1 is oriented toward the edge of mitral annulus (anatomically left or free-wall side). Additionally, the 3D-STE device implicitly identifies the data points by a coordinate pair (z, ϕ) associated to the axial and hoop discretization. Further details are provided in [52–54].

The recorded data are assumed to be representative of the mechanical deformation exhibited by an adult's healthy heart. Two different orientations, namely vertical and horizontal (identified by three points, A, B, C), assumed as the possible placements of the EH device, are adopted, see Figure 7a. The location of the three points during one heartbeat is illustrated in Figure 7b,c, where a horizontal (Figure 7b) and a vertical (Figure 7c) cross-section shows the outer heart profile at the initial time instant of a single heartbeat ($t = 0\,s$, 1), at mid time ($t = 1/2T_{hb}$, 2), and at the time

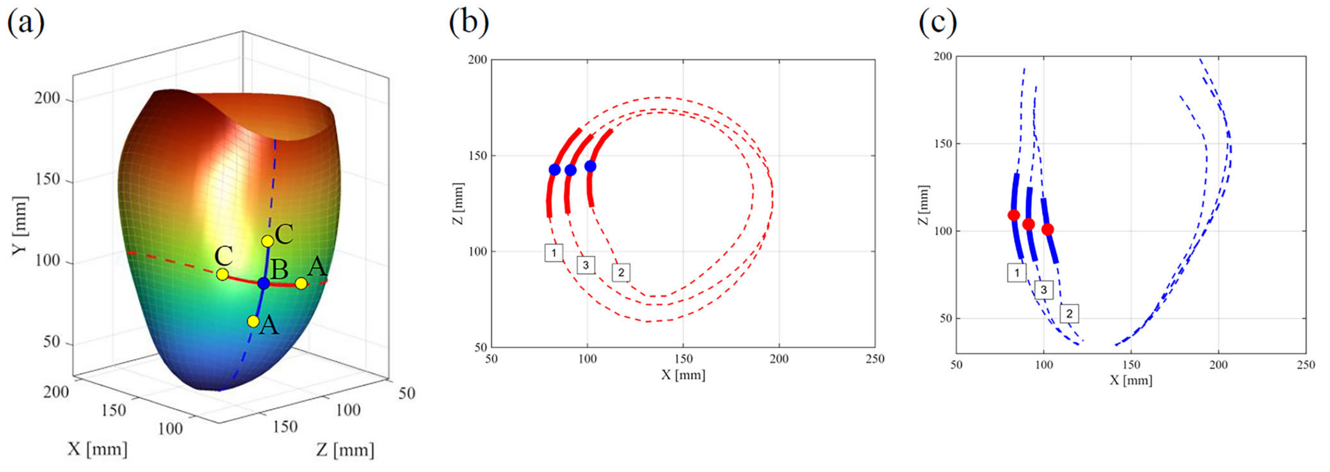

FIGURE 7 | 3D reconstruction of the human heart (a); horizontal (b) and vertical (c) cross sections (see dashed lines in (a)) at three different instants within a single heart beat period, $T_{hb} \cong 0.93$ s: initial time instant 1, 1/2 of the heart beat period 2, and 3/4 of the heart beat period 3, see Figure 8. The positions and directions where the EH devices are supposed to be applied are indicated with the thick red (horizontal) and blue (vertical) segments, while points A, B, and C indicate the extremities and the midpoint of the above segments.

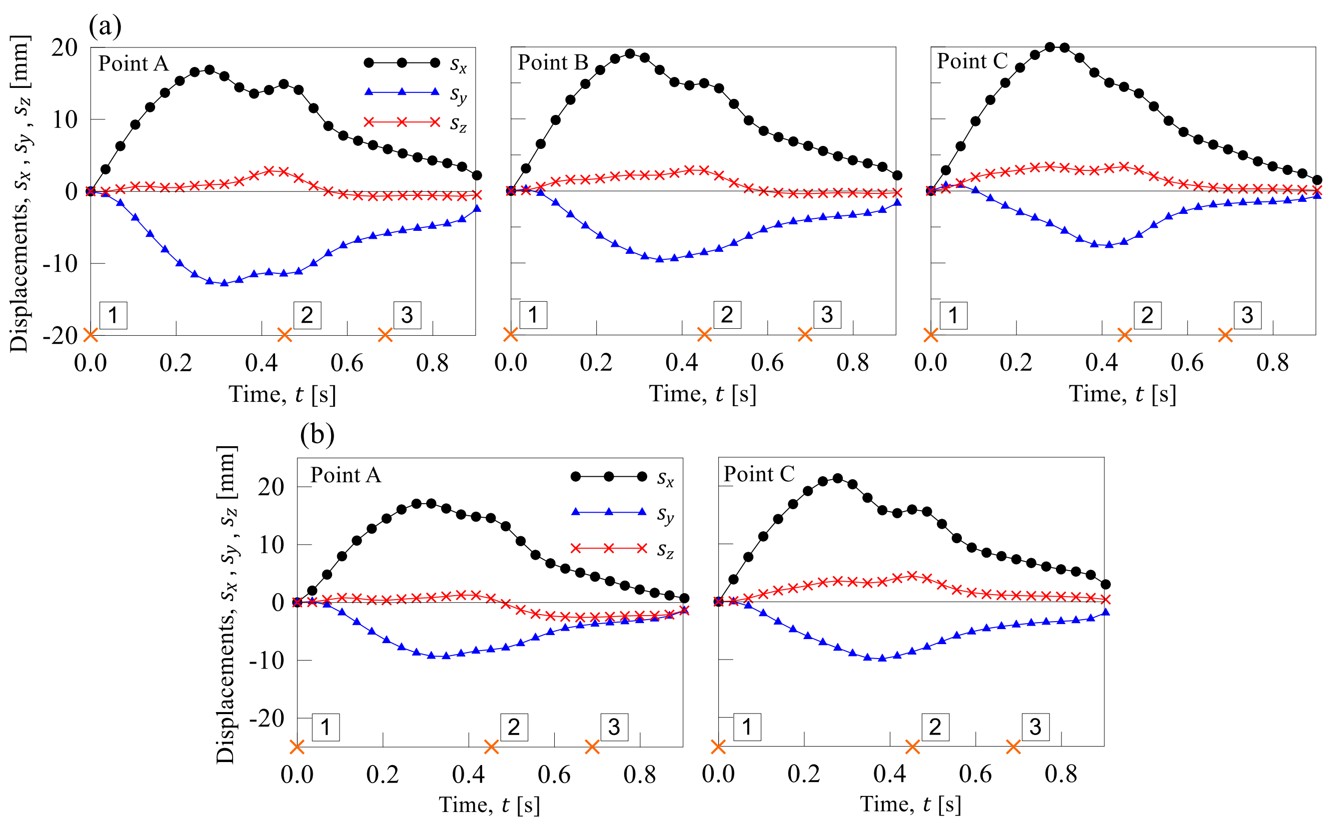

FIGURE 8 | Absolute displacements of the points A, B, and C belonging to the orientation 1 (blue segment, a) and 2 (red segment, b) indicated in Figure 7a; the three considered time instants within one heart-beat period, $T_{hb} \cong 0.93$ s, are indicated as follows: initial time instant 1, 1/2 of the heart beat period 2, and 3/4 of the heart beat period 3.

instant $t = 3/4T_{hb}$ (3) of the heartbeat period T_{hb}. The distance between points A-C is assumed to be roughly equal to 30 mm.

In Figure 8, the components s_x, s_y, s_z of the displacements (referred to the reference system shown in Figure 7a) of the points A, B, C during one heartbeat are shown.

In Figure 9 the relative longitudinal and transversal displacements evaluated for the three points A, B, and C (assumed to be nearly aligned in the reference

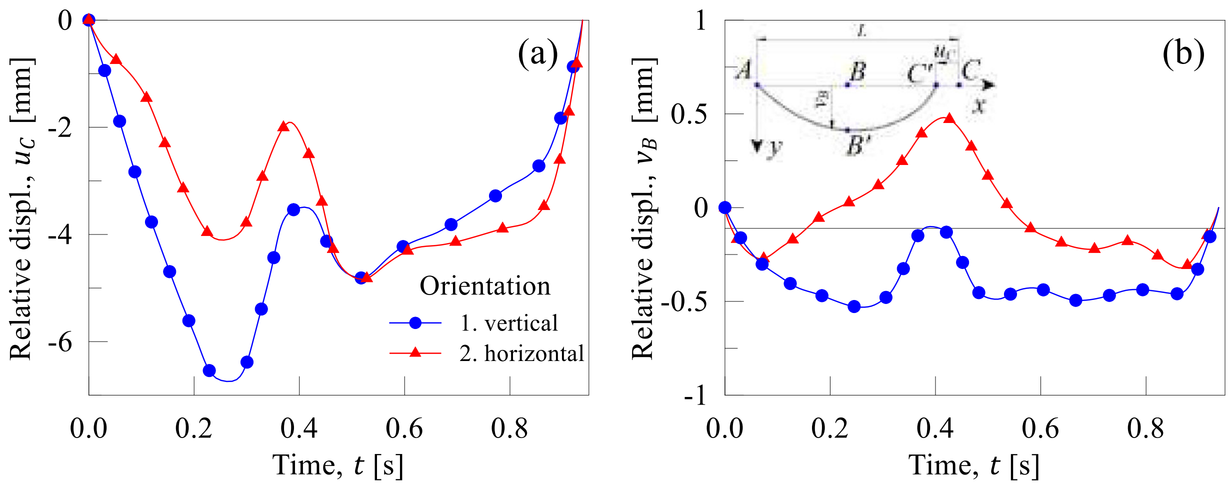

FIGURE 9 | Longitudinal (u_C) (a) and transversal (v_B) (b) displacements evaluated among the points A, B, C lying on the heart surface along the vertical or the horizontal directions (see Figure 7a).

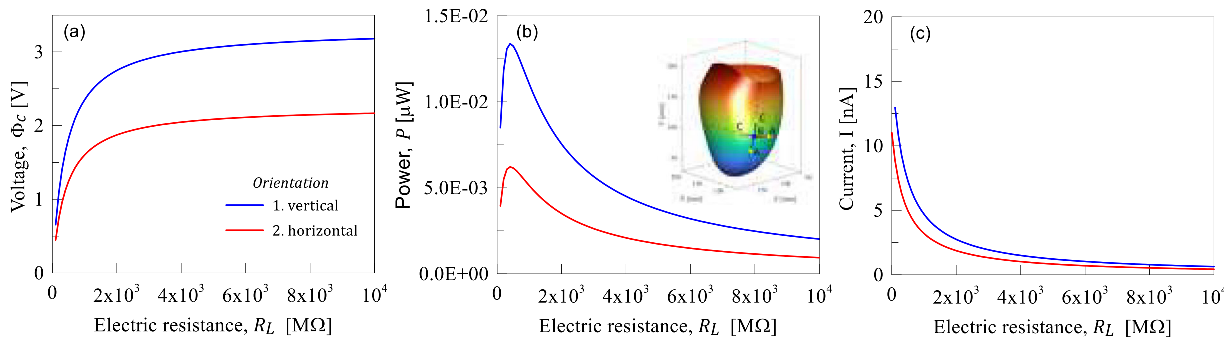

FIGURE 10 | Voltage (a), power (b), and output current (c) obtained through the theoretical model for the relative displacements provided by the motion of the three points lying on the heart surface placed along the vertical and horizontal directions (see Figure 7a) for a wide value range of the load resistance R_L. The real frequency of the heartbeat, f ≅ 1.08 Hz has been used.

configuration, see Figure 7a) during one beat period are illustrated.

6.2 | Electrical Performance of a Heart Motion-driven EH

By using the above-mentioned relative displacements evaluated among the points A, B, and C, the theoretical model is here employed to determine the electric output obtainable from EH3.

As can be observed from the simulation results in Figure 10, the EH placed vertically on the heart surface yields better electrical performance than the horizontally one. The output voltage reaches 2.5 V at a load resistance of 1GΩ. Moreover, for the same load resistance, the output power is 0.016μW, and the output current is 13 nA.

7 | Conclusions

In the present study, we have investigated the energy generation potential of a polymer-based piezoelectric device, employing both single-layer and multilayer architectures. In particular, a novel flexible energy harvester with high output performance was fabricated by connecting in parallel two layers of piezoelectric polyvinylidene fluoride (PVDF), encapsulated within dielectric biocompatible Ecoflex 00–30 films.

Mechanical and electrical experimental measurements, quantifying the output voltage as well as the capacitance and the impedance, have been performed to assess the energy generation capabilities of the EH device. The parallel integration of PVDF layers resulted in enhanced capacitance and reduced impedance, consistent with theoretical expectations for improved charge accumulation and energy transfer efficiency.

Furthermore, a mechanical model of the EH beam-like device has been developed within the large deflection framework, and several parametric analyses have been performed to assess the influence of the frequency of excitation as well as the load electric resistance.

Comparative analysis reveals that the multilayer configuration delivers excellent output performance under bending deformations, underscoring its potential for use in wearable energy harvesters designed to harness energy from natural human motion such as breathing, heartbeats, etc. Future work should focus on optimizing material interfaces to ensure long-term durability and validating energy harvesting efficiency under real-world physiological conditions.

Nomenclature

A_c	Area of the piezoelectric PVDF layer
$\boldsymbol{b}$	Body force vector (force per unit mass)
$\boldsymbol{C}$	Elasticity tensor
C_p	Capacitance of a parallel plate capacitor
$\boldsymbol{d}$, d_{ij}, $\boldsymbol{e}$, e_{ij}	3rd-order piezoelectric constant tensor in the strain-charge and in the stress-charge form, respectively
$\boldsymbol{D}$	Vector of electric displacements
E	Young modulus
$\bar{E}\bar{I}$	Flexural rigidity of the composite beam obtained as the product between the average Young's modulus of the cross section and the weighted average moment of inertia of the beam's cross section
$\boldsymbol{E}$	Electric field
E_n	Energy produced by the EH in one period of the applied cyclic deformation
f	Frequency of the electrical excitation
I	Current intensity
L	Length of the piezoelectric beam
N	Axial force in the composite piezoelectric beam
$\mathbb{p}$, $\mathbb{p}_p$	Polarization vector and permanent polarization vector, respectively
P	Power generated by the EH device connected to a circuit
q_S	Charge per unit surface area
Q_m	Mechanical quality factor quantifying the mechanical energy loss in the piezoelectric material
$\boldsymbol{r}_0(s)$, $\boldsymbol{r}(s)$	Position vector of the centerline of the beam representing the EH device in the reference and in the deformed configuration, respectively
R_{int}	Internal electrical resistance of the piezoelectric device
R_L	Electrical resistance of the load
s	Thickness of the piezoelectric layer
s_x, s_y, s_z,	Displacement components of the heart surface along the coordinate axes
t	Time
$\boldsymbol{t}$, $\bar{\boldsymbol{t}}$	Traction vector, and assigned tractions applied on the portion ∂B_t of the boundary, respectively
T_{hb}	Time period of one heartbeat
$\boldsymbol{u}$, $\bar{\boldsymbol{u}}$	Displacement vector, and known displacement on the portion ∂B_u of the boundary, respectively
$u(s)$, $v(s)$	Longitudinal and transversal displacements of the PVDF beam's centerline, respectively, being s the curvilinear abscissa
w_{PVDF}	Thickness of the PVDF layer
X_C	Capacitive reactance of the EH device
Y	Impedance of the energy harvesting (EH) device
Z	Complex device impedance
ε, ε_{ij}	2nd-order tensor of the dielectric constants
$\boldsymbol{\varepsilon}$	Deformation tensor
ϵ_0, ϵ_r	Electric permittivity of the free space and relative electric permittivity of the material, respectively
$\Phi(\boldsymbol{x}, t)$	Electric potential
Φ_c, Φ_{oc}	Voltage of the actual circuit and that of the open circuit, respectively
$\omega = 2\pi f$	Angular frequency
ρ	Mass density
$\boldsymbol{\sigma}$, $\boldsymbol{\sigma}_M$,$\boldsymbol{\sigma}_E$, $\boldsymbol{\sigma}_p$	Total, mechanical, Maxwell, and piezoelectric Cauchy stress tensor, respectively

Acknowledgements

HE and RB gratefully acknowledge financial support from the European Union's Horizon (HORIZON-MSCA-2023-PF-01, NEW-TECH) under the Marie Skłodowska-Curie grant agreement No. 101147327. We gratefully acknowledge Prof. Lanceros Mendez for the experimental tests performed at BCMaterials (Basque Center on Materials, Spain).

Open access publishing facilitated by Universita degli Studi di Firenze, as part of the Wiley - CRUI-CARE agreement.

Conflicts of Interest

The authors declare no conflicts of interest.

Data Availability Statement

The data that support the findings of this study are available from the corresponding author upon reasonable request.

References

1. E. Abyzova, E. Dogadina, R. D. Rodriguez, et al., "Beyond Tissue Replacement: The Emerging Role of Smart Implants in Healthcare," *Materials Today Bio* 22 (2023): 100784, https://doi.org/10.1016/j.mtbio.2023.100784.

2. N. Sezer and M. Koç, "A Comprehensive Review on the State-of-the-Art of Piezoelectric Energy Harvesting," *Nano Energy* 80 (2021): 105567, https://doi.org/10.1016/j.nanoen.2020.105567.

3. N. Almarri, J. Chang, W. Song, D. Jiang, and A. Demosthenous, "Piezoelectric Energy Harvesting and Ultra-Low-Power Management Circuits for Medical Devices," *Nano Energy* 131 (2024): 110196, https://doi.org/10.1016/j.nanoen.2024.110196.

4. Q. Wang, T. Ruan, Q. Xu, B. Yang, and J. Liu, "Wearable Multifunctional Piezoelectric MEMS Device for Motion Monitoring, Health Warning, and Earphone," *Nano Energy* 89 (2021): 106324, https://doi.org/10.1016/j.nanoen.2021.106324.

5. A. Nechibvute, A. Chawanda, and P. Luhanga, "Piezoelectric Energy Harvesting Devices: an Alternative Energy Source for Wireless Sensors," *Smart Materials Research* 2012, no. 1 (2012): 853481.

6. P. Pillatsch, E. M. Yeatman, A. S. Holmes, and P. K. Wright, "Wireless Power Transfer System for A Human Motion Energy Harvester," *Sensors and Actuators A: Physical* 244 (2016): 77–85, https://doi.org/10.1016/j.sna.2016.04.022.

7. S. Hazra, S. Sengupta, S. Ratha, A. Ghatak, A. K. Raychaudhuri, and B. Ghosh, "Piezoelectric Nanogenerators based on Lead Zirconate Titanate Nanostructures: an Insight into the Effect of Potential Barrier and Morphology on the Output Power Generation," *Nanotechnology* 33, no. 15 (2022): 155403, https://doi.org/10.1088/1361-6528/ac4739.

8. M. Ichiki, K. Ashida, and T. Kitahara, "Characterization of Piezoelectric Lead Zirconate Titanate From the Viewpoint of Transducer and Power Generator Properties," *Japanese Journal of Applied Physics* 41, no. 11S (2002): 7080–7083, https://doi.org/10.1143/JJAP.41.7080.

9. T. D. Usher, K. R. Cousins, R. Zhang, and S. Ducharme, "The Promise of Piezoelectric Polymers," *Polymer International* 67, no. 7 (2018): 790–798, https://doi.org/10.1002/pi.5584.

10. V. O. Concha, L. Timóteo, L. A. Duarte, et al., "Properties, Characterization and Biomedical Applications of Polyvinylidene Fluoride (PVDF): A Review," *Journal of Materials Science* 59, no. 31 (2024): 14185–14204, https://doi.org/10.1007/s10853-024-10046-3.

11. S. Mohammadpourfazeli, S. Arash, A. Ansari, S. Yang, K. Mallick, and R. Bagherzadeh, "Future Prospects and Recent Developments of Polyvinylidene Fluoride (PVDF) Piezoelectric Polymer; Fabrication Methods, Structure, and Electro-Mechanical Properties," *RSC Advances* 13, no. 1 (2023): 370–387, https://doi.org/10.1039/D2RA06774A.

12. H. Kawai, "The Piezoelectricity of Poly (vinylidene Fluoride)," *Japanese Journal of Applied Physics* 8, no. 7 (1969): 975, https://doi.org/10.1143/JJAP.8.975.

13. V. Sencadas, M. V. Moreira, S. Lanceros-Méndez, A. S. Pouzada, and R. Gregório Filho, "α-to β Transformation on PVDF Films Obtained by Uniaxial Stretch," in *Materials Science Forum* (Trans Tech Publications Ltd, 2006), 872–876.

14. S. S. Dani, A. Tripathy, N. R. Alluri, S. Balasubramaniam, and A. Ramadoss, "A Critical Review: The Impact of Electrical Poling on the Longitudinal Piezoelectric Strain Coefficient," *Materials Advances* 3, no. 24 (2022): 8886–8921, https://doi.org/10.1039/D2MA00559J.

15. S. Satapathy, S. Pawar, P. K. Gupta, and K. B. R. Varma, "Effect of Annealing on Phase Transition In Poly(vinylidene fluoride) Films Prepared Using Polar Solvent," *Bulletin of Materials Science* 34 (2011): 727–733, https://doi.org/10.1007/s12034-011-0187-0.

16. K. Lau, Y. Liu, H. Chen, and R. L. Withers, "Effect of Annealing Temperature on the Morphology and Piezoresponse Characterisation of Poly (Vinylidene Fluoride-trifluoroethylene) Films via Scanning Probe Microscopy," *Advances in Condensed Matter Physics* 2013, no. 1 (2013): 435938.

17. A. W. Laramée, C. Lanthier, and C. Pellerin, "Electrospinning of Highly Crystalline Polymers for Strongly Oriented Fibers," *ACS Applied Polymer Materials* 2, no. 11 (2020): 5025–5032, https://doi.org/10.1021/acsapm.0c00873.

18. X. Yuan, Z. Mai, H. Li, et al., "Enhanced Energy Density in Piezoelectric PVDF-Polymer Nanocomposite via Multiple Mechanism Synergetic Action," *Nano Energy* 127 (2024): 109734, https://doi.org/10.1016/j.nanoen.2024.109734.

19. Y. Ting, H. Gunawan, A. Sugondo, and C. W. Chiu, "A New Approach of Polyvinylidene Fluoride (PVDF) Poling Method for Higher Electric Response," *Ferroelectrics* 446, no. 1 (2013): 28–38, https://doi.org/10.1080/00150193.2013.820983.

20. T. Liu, Y. Wang, M. Hong, J. Venezuela, W. Shi, and M. Dargusch, "Advances in Biodegradable Piezoelectrics for Medical Implants," *Nano Today* 52 (2023): 101945, https://doi.org/10.1016/j.nantod.2023.101945.

21. M. Khazaee, A. A. Enkeshafi, S. Riahi, L. Rosendahl, B. Kjærgaard, and A. Rezania, "Contact-Based Impact Energy Harvesting from the Ultralow Frequency Intracardiac Kinetic Energy," *ACS Energy Letters* 9, no. 6 (2024): 2944–2952.

22. Y. Guan, M. Bai, Q. Wang, et al., "A Self-Powered Wearable Piezoelectric Nanogenerator for Physiological Monitoring based on Lead Zirconate Titanate/Microfibrillated cellulose@polyvinyl Alcohol (PZT/MFC@PVA) Composition," *Chemical Engineering Journal* 460 (2023): 141598, https://doi.org/10.1016/j.cej.2023.141598.

23. T. Tsukamoto, Y. Umino, S. Shiomi, K. Yamada, and T. Suzuki, "Bimorph Piezoelectric Vibration Energy Harvester with Flexible 3D Meshed-Core Structure for Low Frequency Vibration," *Science and Technology of Advanced Materials* 19, no. 1 (2018): 660–668, https://doi.org/10.1080/14686996.2018.1508985.

24. Q. Shi, T. Wang, and C. Lee, "MEMS Based Broadband Piezoelectric Ultrasonic Energy Harvester (PUEH) for Enabling Self-Powered Implantable Biomedical Devices," *Scientific Reports* 6, no. 1 (2016): 24946, https://doi.org/10.1038/srep24946.

25. F. Mokhtari, S. Danti, B. Azimi, et al., "Self-Powered Nanostructured Piezoelectric Filaments as Advanced Transducers for New Cochlear Implants," *Energy & Environmental Materials* 8, no. 1 (2025): 12807, https://doi.org/10.1002/eem2.12807.

26. J. Liu, B. Yang, L. Lu, et al., "Flexible and Lead-Free Piezoelectric Nanogenerator as Self-Powered Sensor based on Electrospinning BZT-BCT/P(VDF-TrFE) Nanofibers," *Sensors and Actuators A: Physical* 303 (2020): 111796, https://doi.org/10.1016/j.sna.2019.111796.

27. A. Pal, A. Sasmal, B. Manoj, D. P. Rao, A. K. Haldar, and S. Sen, "Enhancement in Energy Storage and Piezoelectric Performance of Three Phase (PZT/MWCNT/PVDF) Composite," *Materials Chemistry and Physics* 244 (2020): 122639, https://doi.org/10.1016/j.matchemphys.2020.122639.

28. Q. Zheng, B. Shi, F. Fan, et al., "In Vivo Powering of Pacemaker by Breathing-Driven Implanted Triboelectric Nanogenerator," *Advanced Materials* 26, no. 33 (2014): 5851–5856, https://doi.org/10.1002/adma.201402064.

29. C. Dagdeviren, B. D. Yang, Y. Su, et al., "Conformal Piezoelectric Energy Harvesting and Storage From Motions of the Heart, Lung, and Diaphragm," *Proceedings of the National Academy of Sciences* 111, no. 5 (2014): 1927–1932, https://doi.org/10.1073/pnas.1317233111.

30. C. Hu, K. Behdinan, and R. Moradi-Dastjerdi, "PVDF Energy Harvester for Prolonging the Battery Life of Cardiac Pacemakers," *Actuators* 11, no. 7 (2022): 187, https://doi.org/10.3390/act11070187.

31. B. Lu, Y. Chen, D. Ou, et al., "Ultra-flexible Piezoelectric Devices Integrated With Heart to Harvest the Biomechanical Energy," *Scientific Reports* 5, no. 1 (2015): 16065, https://doi.org/10.1038/srep16065.

32. J. Li, T. A. Hacker, H. Wei, et al., "Long-Term In Vivo Operation of Implanted Cardiac Nanogenerators in Swine," *Nano Energy* 90 (2021): 106507, https://doi.org/10.1016/j.nanoen.2021.106507.

33. L. Dong, A. B. Closson, M. Oglesby, et al., "In Vivo Cardiac Power Generation Enabled by an Integrated Helical Piezoelectric Pacemaker Lead," *Nano Energy* 66 (2019): 104085, https://doi.org/10.1016/j.nanoen.2019.104085.

34. Z. Xu, C. Jin, A. Cabe, et al., "Flexible Energy Harvester on a Pacemaker Lead Using Multibeam Piezoelectric Composite Thin Films," *ACS Applied Materials & Interfaces* 12, no. 30 (2020): 34170–34179, https://doi.org/10.1021/acsami.0c07969.

35. E. J. Shin, C. Prasad, and H. Y. Choi, "Recent Advances in Thermoplastic Polyurethane-based Composites, Properties, Synthesis and its Applications," *Journal of Industrial and Engineering Chemistry* 156 (2026): 150–191, https://doi.org/10.1016/j.jiec.2025.09.009.

36. D. Haojiang, "General Solutions for Coupled Equations for Piezoelectric Media," *International Journal of Solids and Structures* 33, no. 16 (1996): 2283–2298, https://doi.org/10.1016/0020-7683(95)00152-2.

37. G. C. Patil, "Doctor Blade: A Promising Technique for Thin Film Coating," *Simple Chemical Methods for Thin Film Deposition: Synthesis and Applications* (Singapore: Springer Nature Singapore, 2023), 509–530, https://doi.org/10.1007/978-981-99-0961-2.

38. Z. Xu, S. Zheng, X. Wu, et al., "High Actuated Performance MWCNT/Ecoflex Dielectric Elastomer Actuators based on Layer-By-Layer Structure," *Composites Part A: Applied Science and Manufacturing* 125 (2019): 105527, https://doi.org/10.1016/j.compositesa.2019.105527.

39. M. Samet, A. Kallel, and A. Serghei, "Maxwell-Wagner-Sillars Interfacial Polarization in Dielectric Spectra of Composite Materials: Scaling Laws and Applications," *Journal of Composite Materials* 56, no. 20 (2022): 3197–3217, https://doi.org/10.1177/00219983221090629.

40. K. Lee, Y. Jeong, C. H. Lee, J. Lee, H. S. Seo, and Y. Cho, “Impedance Coupled Voltage Boosting Circuit for Polyvinylidene Fluoride Based Energy Harvester,” *Sensors* 23, no. 1 (2022): 137, https://doi.org/10.3390/s23010137.

41. N. M. Morris, *Mastering Electronic and Electrical Calculations* (Macmillan, 1996), 86–101, https://doi.org/10.1007/978-1-349-13705-3.

42. H. Narayanan, “On the Maximum Power Transfer Theorem,” *International Journal of Electrical Engineering & Education* 15, no. 2 (1978): 161–167, https://doi.org/10.1177/002072097801500211.

43. J. Song, G. Zhao, B. Li, and J. Wang, “Design Optimization of PVDF-based Piezoelectric Energy Harvesters,” *Heliyon* 3, no. 9 (2017): e00377, https://doi.org/10.1016/j.heliyon.2017.e00377.

44. M. Koç, “Effect of Multilayer Fabrication of PVDF/PZT Fibers on Output Performance in Piezoelectric Nanogenerator (PEN),” *Journal of Polymer Research* 31, no. 6 (2024): 160.

45. S. Gupta, R. Bhunia, B. Fatma, et al., “Multifunctional and Flexible Polymeric Nanocomposite Films With Improved Ferroelectric and Piezoelectric Properties for Energy Generation Devices,” *ACS Applied Energy Materials* 2, no. 9 (2019): 6364–6374, https://doi.org/10.1021/acsaem.9b01000.

46. A. Zargarani and S. N. Mahmoodi, “Enhancing the Output Power of a Piezoelectric Energy Harvester by Reducing the Effect of the Internal Capacitance Using Inductance,” *Smart Materials, Adaptive Structures and Intelligent Systems* (American Society of Mechanical Engineers, 2016), V002T07A014.

47. J. Song, G. Zhao, B. Li, and J. Wang, “Design Optimization of PVDF-based Piezoelectric Energy Harvesters,” *Heliyon* 3, no. 9 (2017): e00377, https://doi.org/10.1016/j.heliyon.2017.e00377.

48. T. Hanuhov and N. Cohen, “Thermally Induced Deformations in Multi-Layered Polymeric Struts,” *International Journal of Mechanical Sciences* 215 (2022): 106959, https://doi.org/10.1016/j.ijmecsci.2021.106959.

49. T. Hanuhov and N. Cohen, “Design Principles for 3D-Printed Thermally Activated Shape-Morphing Structures,” *International Journal of Mechanical Sciences* 262 (2024): 108716, https://doi.org/10.1016/j.ijmecsci.2023.108716.

50. Y. H. Shin, I. Jung, H. Park, et al., “Mechanical Fatigue Resistance of Piezoelectric PVDF Polymers,” *Micromachines* 9, no. 10 (2018): 503, https://doi.org/10.3390/mi9100503.

51. D. Mao, I. Mejia, H. Stiegler, B. E. Gnade, and M. A. Quevedo-Lopez, “Fatigue Characteristics of Poly(Vinylidene Fluoride-Trifluoroethylene) Copolymer Ferroelectric Thin Film Capacitors for Flexible Electronics Memory Applications,” *Organic Electronics* 12, no. 8 (2011): 1298–1303, https://doi.org/10.1016/j.orgel.2011.04.011.

52. P. Piras, L. Teresi, P. E. Puddu, et al., “Morphologically Normalized Left Ventricular Motion Indicators from MRI Feature Tracking Characterize Myocardial Infarction,” *Scientific Reports* 7, no. 1 (2017): 12259, https://doi.org/10.1038/s41598-017-12539-5.

53. V. Varano, P. Piras, S. Gabriele, et al., “Local and Global Energies for Shape Analysis in Medical Imaging,” *International Journal for Numerical Methods in Biomedical Engineering* 36, no. 2 (2020): 3252, https://doi.org/10.1002/cnm.3252.

54. J. I. Colorado-Cervantes, P. Nardinocchi, P. Piras, et al., “Patient-Specific Modeling of Left Ventricle Mechanics,” *Acta Mechanica Sinica* 38, no. 1 (2022): 621211, https://doi.org/10.1007/s10409-021-09041-0.